Concours externe Inria 2014

Arrêté du 18 avril 2014

Poste « COM 1 : Responsable communication (H/F) »

Accès au corps des Ingénieurs d'étude

Epreuve du 25 juin 2014
Note sur 20 – Coefficient 3 – Durée 3 heures

****

La notation prendra en compte la qualité des réponses, mais aussi la rédaction, la présentation, le style et l'orthographe.

Veuillez respecter l'anonymat dans les réponses.

Ne pas omettre de noter votre numéro d'ordre sur les feuilles intercalaires.

Les documents et calculatrice ne sont pas autorisés.

Barème de notation

Question 1 : 6 points

Question 2 : 8 points

Question 3 : 6 points

Les questions sont indépendantes les unes des autres.

Vous êtes responsable de communication de l'un des centres de l'ERPI, établissement de recherche public organisé en 10 centres répartis sur le territoire national. Chaque centre est composé de 20 à 30 équipes de recherche et de services d'appui : service administratif, financier, informatique, ressources humaines, communication, qui apportent leur soutien aux activités des équipes de recherche et au fonctionnement du centre.

Une équipe de recherche réunit autour d'une personnalité scientifique, une vingtaine de collaborateurs : scientifiques confirmés, ingénieurs, doctorants, post---doctorants originaires des cinq continents. Ces collaborateurs ont souvent des statuts différents, ils peuvent être agents de l'établissement, fonctionnaires ou CDD, ou salariés d'établissements partenaires (autre centre de recherche, grande école, université..). Les équipes de recherche peuvent être mono---localisées sur un des 10 centres de recherche, bi---localisées entre un centre de recherche et un partenaire sur un site distant ou totalement hébergées chez un partenaire sur un site distant.

Quelle que soit leur localisation, les équipes de recherche d'un centre sont soutenues par les services du centre.

Question 1

Votre directeur vous donne comme objectif de renforcer la cohésion entre les différentes équipes de recherche quelle que soit leur localisation.

a) Dans le cas d'équipes de recherche hébergées chez un partenaire sur un site distant, quels risques identifiez vous, décrivez le volet de votre plan de communication interne répondant à cette problématique.

b) Vous proposerez plusieurs types d'actions et décrirez en détail un de ces types d'actions.

Question 2

Vous recevez un mail (annexe page 4), qui témoigne d'échanges entre des chercheurs et différents interlocuteurs. Un communiqué de presse est envisagé par les chercheurs, qui souhaitent mettre en valeur un beau résultat de recherche ayant fait l'objet d'un article dans la fameuse revue scientifique *Nature* (annexe page 7).

a) Quelle est votre recommandation aux chercheurs pour valoriser ce travail? Présentez votre argumentation.

b) Vous êtes amené à évoquer le sujet en quelques phrases au responsable de l'Espace des Sciences qui est un centre d'exposition et de conférence local. Comment le présentez---vous ?

c) Rédigez une brève pour le site institutionnel de l'ERPI (une centaine de mots).

Questions 3

Créé en 1967, l'ERPI prévoit de fêter ses 50 ans en 2017. Dans chacun de ses 10 centres de recherche, cette année anniversaire sera jalonnée de temps forts ayant pour objectifs de renforcer les liens avec les partenaires locaux et de faire rayonner les centres ERPI dans leur environnement local.
La direction nationale de la communication qui comprend une équipe de réalisation audio---visuelle, un pôle digital et un pôle conception---édition, souhaite anticiper au mieux le support humain et financier qu'elle pourra apporter aux centres et demande au responsable de communication de chacun des 10 centres de proposer des actions qui pourront avoir lieu dans son centre.
Les actions proposées doivent mettre en valeur l'activité de recherche et d'innovation, passée et présente des chercheurs du centre et également renforcer la communication interne.

En 50 ans, l'ERPI s'est progressivement installé et déployé sur le territoire national. En 2014, votre centre de recherche, comme les neuf autres centres de l'ERPI a cessé de croître, il a atteint son rythme de croisière.
Il rassemble des équipes de recherche historiques, mais également des équipes plus récentes. Les recherches menées dans votre centre se caractérisent par des travaux préfigurant la mise au point d'internet, les sciences informatiques pour l'aérospatiale ou l'aéronautique ; la recherche fondamentale sur les langages formels et les langages de programmation, l'algorithmique et les preuves de programmes mais aussi recherche appliquée principalement dans les domaines suivants : gestion de la dépollution, véhicules intelligents, logiciels pour la création musicale. Cette recherche réalisée au sein du centre se place au plus haut niveau international. Elle a contribué à la notoriété scientifique de l'ERPI et a également permis de belles innovations : logiciels, plateformes, protocoles standards, et produits portés par des start---up.

Décrivez la feuille de route de com "ERPI 2017 pour votre centre" que vous avez validée avec votre directeur de centre et que vous proposez de présenter à la direction de la communication, en précisant :
--- les objectifs propres au centre, dans cet
anniversaire --- un programme prévisionnel pour
l'année 2017 --- des estimations budgétaires,
--- un planning

Vous préciserez les actions qui peuvent être mutualisées entre plusieurs centres.

------o0o—

ANNEXE

From : Olivier.Quicherch@erpi.fr

To : Sylvie.Lacom@cnrs.fr
Cc : Pierre.Comain@erpi.fr, Pauline.Autrecom@erpi.fr, Miranda.Fictive@cnrs.fr

Bonjour,

Je suis entièrement d'accord avec Miranda. J'ajoute en outre qu'il s'agit d'un travail pluridisciplinaire par excellence, illustrant les découvertes que l'on peut faire en combinant du phénotypage, de la biologie moléculaire, de la microscopie laser, des mathématiques des statistiques et de l'informatique, le tout dans une approche navigant à travers les échelles (de la molécule à la plante entière en passant par le méristème et ses organes). C'est aussi un travail associant de façon essentielle des compétences de deux instituts de recherche français dans des disciplines très différentes (biologie et mathématique/informatique). Cela préfigure sans doute ce vers quoi évolueront la biologie ET l'informatique de demain...

Comme l'a dit Miranda, ces travaux ont été largement anticipés par des mathématiciens/informaticiens célèbres comme Turing qui a fait une contribution remarquable au décodage de l'énigme de la phyllotaxie. Notre papier contribue (modestement) à continuer de lever le voile.

Bien cordialement

Olivier

From : Miranda.Fictive@cnrs.fr

To : Sylvie.Lacom@cnrs.fr
Cc : Pierre.Comain@erpi.fr, Pauline.Autrecom@erpi.fr
Le 7 nov. 2013 à 18:27,

Bonsoir,

Je vais évidemment plaider pour ma chapelle mais je trouve cela extrêmement dommage que vous n'envisagiez pas de communiqué de presse autour de ce papier surtout conjointement entre nos 2 établissements.

La phyllotaxie est un sinon le plus vieux champ de recherche interdisciplinaire (qui a même été à l'origine du développement de la cristallographie). La régularité du phénomène et le fait que les angles entre les fleurs sont de 137° c'est à dire l'angle d'or défini à partir de la suite de Fibonacci ont en effet attiré physiciens, mathématiciens et biologistes depuis plusieurs siècles.

C'est ainsi un des plus jolis exemples d'auto-organisation dans le monde biologique qui a inspiré les travaux de Turing sur la morphogenèse (qui préparait un article sur ce sujet au moment de sa mort).

Les résultats de ce travail vont donc bien au delà d'un simple problème "végétal" mais touche vraiment à l'essence même du développement c'est à dire comment générer de la complexité à partir d'information de départ relativement simple. Il n'y a pas d'autres exemples connus dans le monde vivants où deux champs régulateurs de la signalisation permettent de conduire à l'émergence rythmique de structure avec un contrôle spatio-temporelle précis. Le paradigme à l'heure actuel un contrôle par une horloge moléculaire tel que cela est observé pour la segmentation chez les animaux (production des somites) et également chez les plantes pour la production des racines latérales. Dans le cas de la phyllotaxie nous avons deux champs qui combinés génèrent cette rythmicité: l'horloge n'est plus interne aux cellules mais émerge au niveau tissulaire. Et pour comprendre ce système, nous avons été les premiers à observer ce système vivant sur de longues périodes afin de comprendre comment il s'auto-organise. Et nous montrons également comment des défauts dans la temporalité de la morphogenèse se répercutent sur l'architecture de la plante en identifiant une signature, c'est à dire un défaut caractéristique dans la distribution des fleurs sur la tige.

Ce travail est ainsi également le premier qui permet d'accéder à une vision multi-échelle de la construction de la partie aérienne d'un organisme végétale. Et ce travail n'aurait pas été possible sans une équipe composée de biologistes, de mathématiciens, de modélisateurs et de physiciens!

Ce n'est pas des choses que j'ai forcément mis en avant dans le texte initial que j'ai fourni (ne sachant pas ce que ce texte allait devenir) mais il me semble qu'il y a tout à fait matière à faire un texte qui pourrait toucher un public plus large qu'une communauté de spécialistes.

Une de mes thésardes, Sabrina R., vient de recevoir un prix de la Fondation L'Oréal-L'Unesco, pour son travail sur ce système biologique unique. Cela illustre je pense la portée large que peuvent avoir ces travaux.

Bien à vous

Miranda

From : Sylvie.Lacom@cnrs.fr
To : Miranda.Fictive@cnrs.fr
Cc : Pierre.Comain@erpi.fr, Pauline.Autrecom@cnrs.fr
Le 7 nov. 2013 à 10:54,

Bonjour,

Le CNRS a choisi de valoriser ces travaux, non pas sous la forme d'un communiqué de presse mais d'une actualité des laboratoires. Celle-ci sera publiée sur le site du laboratoire et figurera dans la lettre « *En direct de nos labos* » envoyée tous les quinze jours à plus de 450 journalistes.

Bien à vous,

Sylvie L.

From : Miranda.Fictive@cnrs.fr

To : Sylvie.Lacom@cnrs.fr
Cc : Pierre.Comain@erpi.fr, Pauline.Autrecom@erpi.fr
Le 7 nov. 2013 à 10:27

Bonjour Sylvie,

A propos de la communication autour du papier dans Nature à venir, notre collaboration avec l'équipe de recherche ERPI de Montpellier a joué un rôle clé dans ce travail et je voudrais donc mettre l'ERPI dans la boucle. Je mets en CC les deux interlocuteurs com de l'ERPI pour prise de contact.

A bientôt

Miranda

NATURE International weekly journal of science

Nature Letter

Cytokinin signalling inhibitory fields provide robustness to phyllotaxi

Fabrice Besnard, Yassin Refahi, Valérie Morin, Benjamin Marteaux, Géraldine Brunoud, ……Miranda.Fictive, Sylvie Inventer, Christophe Godin, Jan Traas, Yann Guédon & Teva Vernoux

Nature 505, 417–421, (16 January 2014) doi:10.1038/nature12791
Received 12 March 2013; Accepted 17 October 2013; Published online 15 December 2013

How biological systems generate reproducible patterns with high precision is a central question in science[1]. The shoot apical meristem (SAM), a specialized tissue producing plant aerial organs, is a developmental system of choice to address this question. Organs are periodically initiated at the SAM at specific spatial positions and this spatiotemporal pattern defines phyllotaxis. Accumulation of the plant hormone auxin triggers organ initiation[2, 3, 4, 5], whereas auxin depletion around organs generates inhibitory fields that are thought to be sufficient to maintain these patterns and their dynamics[4, 6, 7 , 8, 9, 10, 11 , 12, 13]. Here we show that another type of hormone-based inhibitory fields, generated directly downstream of auxin by intercellular movement of the cytokinin signalling inhibitor *ARABIDOPSIS* HISTIDINE PHOSPHOTRANSFER PROTEIN 6 (AHP6)[14], is involved in regulating phyllotactic patterns. We demonstrate that AHP6-based fields establish patterns of cytokinin signalling in the meristem that contribute to the robustness of phyllotaxis by imposing a temporal sequence on organ initiation. Our findings indicate that not one but two distinct hormone -based fields may be required for achieving temporal precision during formation of reiterative structures at the SAM, thus indicating an original mechanism for providing robustness to a dynamic developmental system.

In the most widely accepted theory for phyllotaxis, spatiotemporal patterns of organ initiation at the SAM result from the combined effect of inhibitory fields produced by existing organs. As these organs are displaced away from the SAM by growth, new organs form sequentially at positions where the sum of the inhibitory effects is the lowest[6, 7, 8]. Both the position of new organs and the time delay between organ initiations (or plastochron) are emergent parameters of this dynamical system[8]. Strong evidence indicates that, notably through a network of polarly localized PIN -FORMED 1 (PIN1) efflux carriers, polar auxin transport not only controls accumulation of auxin at the site of organ initiation but also creates inhibitory fields around organs by auxin depletion[4, 9, 10, 11, 12, 13]. It has therefore been proposed that the auxin

transport system could be sufficient to control both the spatial and the temporal dynamics of phyllotaxis[4].

Here we re-evaluated this proposition by considering the role of cytokinin during organ initiation in *Arabidopsis thaliana*. Cytokinin regulates the size of the stem cell niche (and thus of the SAM) and this can effect phyllotaxis by modifying the geometry of the SAM[15, 16]. To explore a possible role of cytokinin directly in organ initiation, we re-analysed recent transcriptomic data for different domains of the SAM[17] and identified *AHP6* (ref. 14) as the only candidate gene encoding a cytokinin signalling effector specifically enriched in organs (Fig. 1a, Supplementary Figs 1 and 2a). Using *in situ* hybridization, we confirmed that *AHP6* is specifically expressed during organ initiation and development (Fig. 1b, c, Supplementary Fig. 2b–h)[18]. Wild-type *Arabidopsis* plants display spiral phyllotaxis, resulting in consecutive organs generally distributed on the stem at a divergence angle close to a 137.5° canonical angle (noted as α Fig. 1d). In contrast, both *ahp6-1* and *ahp6-3* null mutants as well as the *ahp6-1*/*ahp6-3* (*ahp6-1/3*) trans-heterozygote showed obvious modifications in organ arrangements along the stem (Fig. 1e–g). We also observed supernumerary petals and sepals in flowers (Supplementary Fig. 3), indicating that *AHP6* regulates phyllotaxis throughout inflorescence development.

Figure 1: *AHP6* is expressed in lateral organs and regulates inflorescence architecture.

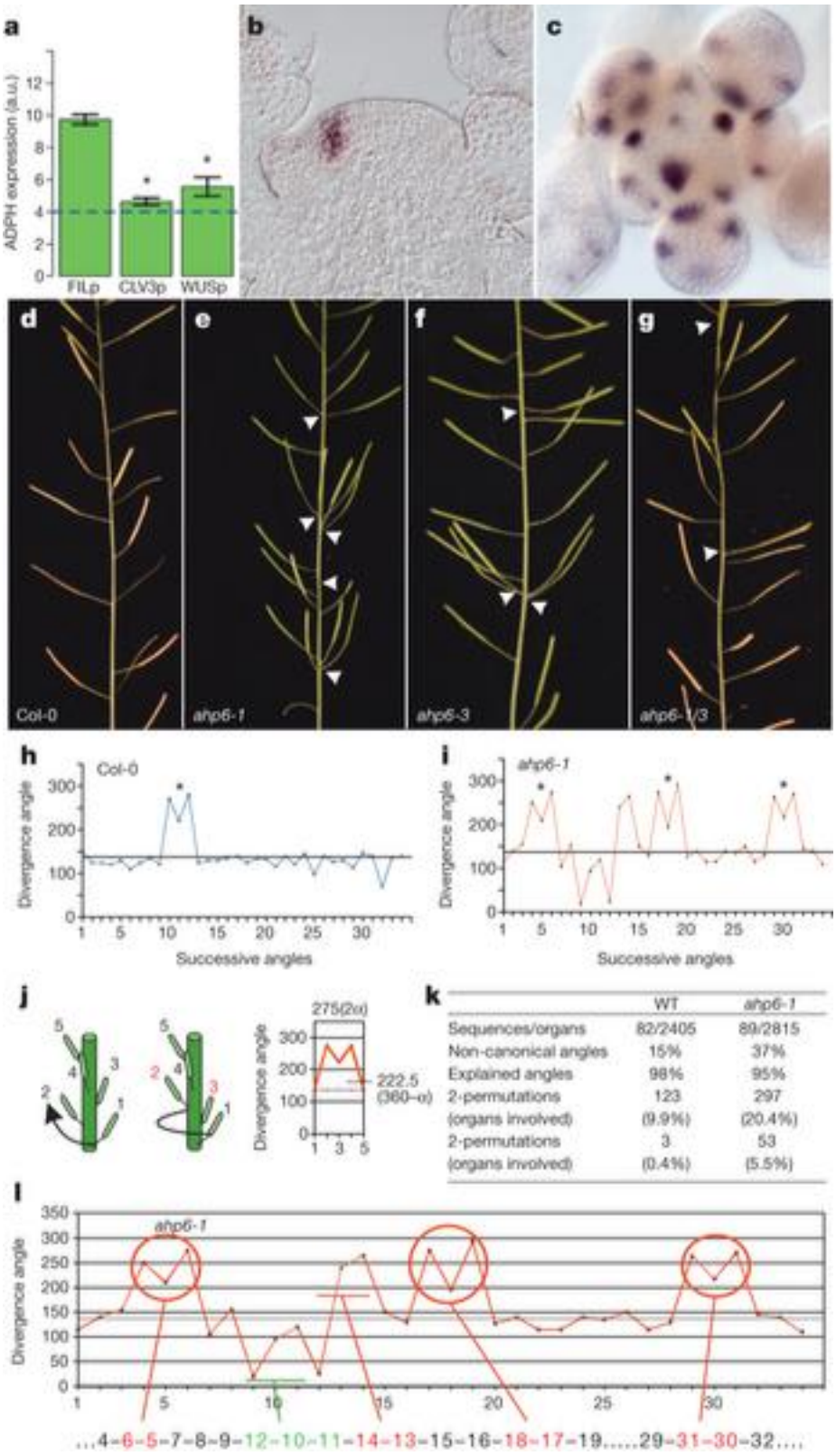

a, *AHP*6 (AT1G80100) expression in genome-wide data for lateral organs (FILp), stem cells (CLV3p) and the WUSCHEL domain (WUSp)[17]. An asterisk indicates statistically different from FILp (Methods). Dashed line indicates non-specific background level. Expression measured in arbitrary units (a.u.). **b**, **c**, *AHP6 in situ* hybridization on section (**b**) and whole-

mount tissues (**c**). **d**–**g**, Wild-type (**d,** Col-0) and *ahp6* (**e**–**g**) inflorescences. Arrowheads (**d**–**g**) indicate perturbations. **h**, **i**, Representative angle sequences for wild type (**h**, *n* = 82) and *ahp6-1* (**i**, *n* = 89). Asterisk indicates M-shaped motif. **j**, Explaining the M-shaped motif: canonical insertion order (left), the one obtained by permutating two organs (centre) and angle sequences (right). **k**, Quantification of permutations. Wild type (WT). **l**, Permutations in the *ahp6-1* sequence from (**i**).

To further characterize the stem architecture of *ahp6* mutants, we analysed sequences of successive divergence angles between organs on the inflorescence stems from a large population of *ahp6-1* and wild-type plants. This analysis demonstrated a notable amount of non-canonical divergence angles in wild-type plants and a large increase in the occurrence of such angles in most mutants (Supplementary Fig. 4a, b). Notably, an 'M-shaped' motif corresponding approximately to the angle sequence 2α, $360-\alpha$, 2α appeared much more frequently in *ahp6* than in wild-type sequences (Fig. 1h, i and Supplementary Fig. 4c–f). It was not associated with changes in the structure of the stem, such as twisting, that could modify angles between siliques (Supplementary Fig. 5). This motif can theoretically arise if two consecutive organs in a canonical sequence are permuted along the stem (Fig. 1j)[19]. By applying a stochastic and a combinatorial model to analyse the divergence angle sequences (see Methods), we showed that over 95% of the non-canonical angles can indeed be explained by permutations of the insertion order of 2 to 3 organs in both wild-type and *ahp6* plants (Fig. 1k, l and Supplementary Fig. 4c–f). We further demonstrated an increase by 2.4-fold and 17.6-fold of permutations involving 2 and 3 organs, respectively, in *ahp6* mutants compared to wild-type plants (Fig. 1k). Altogether, our data indicate that *AHP6* is required for buffering an intrinsic instability of phyllotaxis leading to permutations in the order of organ insertions along the stem.

We next used scanning electron microscopy (SEM) to study the geometry of the *ahp6* mutant SAM. In wild-type meristems the spatial organization of the organs usually followed the expected phyllotaxis and consecutive organs showed clear differences in size (Fig. 2a). In contrast, pairs or triplets of young organs at quasi-identical developmental stages occurred in most *ahp6* meristems (Fig. 2b). This observation was confirmed using a *LEAFY* (*LFY*) promoter driving GFP (*pLFY::GFP*) flower-specific marker line (Fig. 2c, d), demonstrating that the loss of *AHP6* leads to simultaneous development of flowers instead of the mostly sequential outgrowth observed in wild-type meristems. As the size of the stem-cell niche and of the meristem were not significantly affected by the *ahp6* mutation (Supplementary Fig. 6), these data indicate that *AHP6* is required for regulating the sequence of organ initiation and/or organ growth following initiation to restrict concomitant development of organs.

Figure 2: *AHP6* regulates the plastochron.

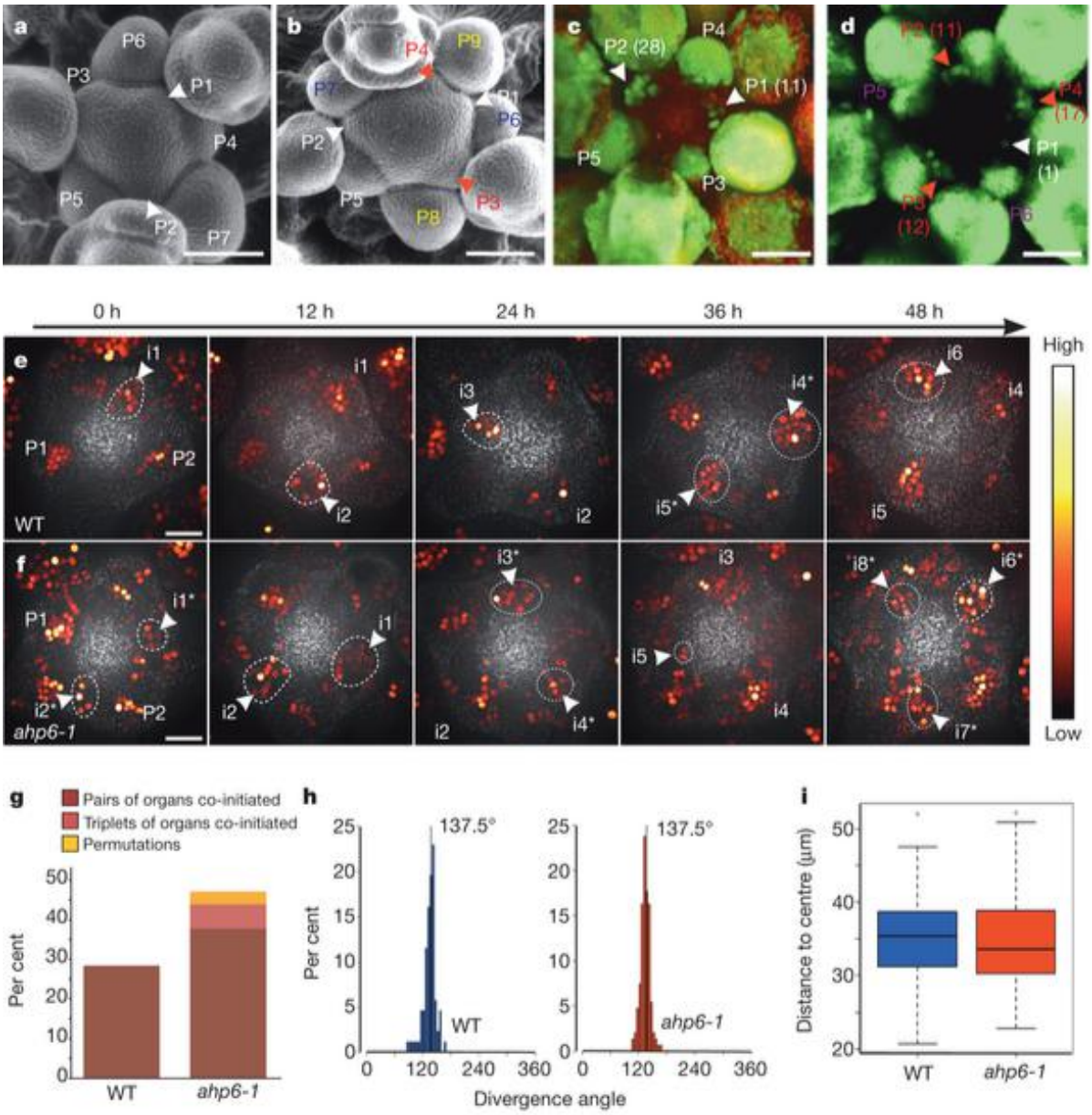

a, **b**, SEM of wild type (**a**, *n* = 15) and *ahp6-1* (**b**, *n* = 17). Letters of identical colours (except white) indicate morphologically identical stages. **c**, **d**, *pLFY::GFP* expression in wild type (**c**) and *ahp6-1* (**d**). Numbers within the brackets indicate number of cells. **e**–**i**, Organ initiation timing and position in wild type (*n* = 20) and *ahp6-1* (*n* = 33) expressing *DR5::VENUS*. Representative time courses (**e**, wild type; **f**, *ahp6-1*); organ co-initiations/permutations (**g**); relative angles (**h**); and radial position of initiation (**i**). Primordia (P) numbered from youngest to oldest, initia (**i**) from oldest to youngest. Asterisks indicate co-initiated organs. Autofluoresence visible in red (**c**, **d**) or grey channels (**e**, **f**). Scale bars, 50 µm (**a**–**d**) or 20 µm

To discriminate between these possible scenarios, we followed the expression of a nuclear-localized *DR5::VENUS*[5] over several days in *ahp6* and wild-type meristems. The synthetic auxin-inducible *DR5* reporter allows monitoring of the recruitment of organ founder cells starting from initium i1 and in primordia from early P1 onwards (Supplementary Fig. 7)[5, 9, 11, 20]. Live imaging of *DR5::VENUS* demonstrated that, although the mean rate of organ

initiation (the mean plastochron) is comparable in wild-type and *ahp6* (Supplementary Fig. 8), the loss of *AHP6* results in a strong increase in concomitant organ initiation and, at a very low frequency (8 out of 255 initiation events), in permutations in the order of organ initiation (Fig. 2e–g and Supplementary Fig. 9). On the contrary, the relative angle between organs and the position of their initiation relative to the centre of the meristem were unaffected by the *ahp6* mutation (Fig. 2h, i). In addition, co-initiated organs were also generated at a similar radial distance from the centre independently of the genotype and with a standard deviation smaller than one cell diameter (Supplementary Fig. 10a)[21] . The rate of organ displacement away from the centre of the SAM was also similar between *ahp6* and wild-type, indicating that AHP6 does not influence growth (Supplementary Fig. 10b). Thus, although organs are initiated at a precise radial distance and with a precise divergence angle, frequent organ co-initiations are observed, indicating an irregular plastochron. *AHP6* is then required to stabilize the plastochron by limiting organ co-initiations. Our data further indicate that organ permutations on the stem result mostly from organ co-initiations. Also, the frequency of perturbations in the sequence of organ initiation at the SAM is higher than the frequency of permutations on the stem in both wild-type and *ahp6* (28% and 47% compared to 10% and 25% for wild-type and *ahp6*, respectively). This indicates that co-initiated organs are sorted when the internode is established either in a normal or in an inverted order, only the latter resulting in permutations on the inflorescence stem.

As auxin activates directly *AHP6* transcription in root tissues[22], we next investigated whether the spatiotemporal pattern of *AHP6* transcription in the SAM could be controlled by auxin. Co-visualization of a *pAHP6::GFP* transcriptional reporter that recapitulates *AHP6* expression pattern (Fig. 3a) and *DR5::VENUS* showed that *AHP6* is activated one plastochron after *DR5* activation (Fig. 3b–d and Supplementary Video 1). *AHP6* expression in the SAM was also lost in *monopteros* (*mp*), a mutant in a major transcriptional effector of auxin signalling in the SAM (Fig. 3e)[23]. In addition, using electrophoretic mobility shift assays (EMSAs), we mapped binding of MONOPTEROS to three out of six locations of putative ARF binding sites in the *AHP6* promoter (Fig. 3f). This indicates that *AHP6* is activated downstream of auxin by MONOPTEROS.

Figure 3: AHP6 acts non---cell---autonomously downstream of auxin.

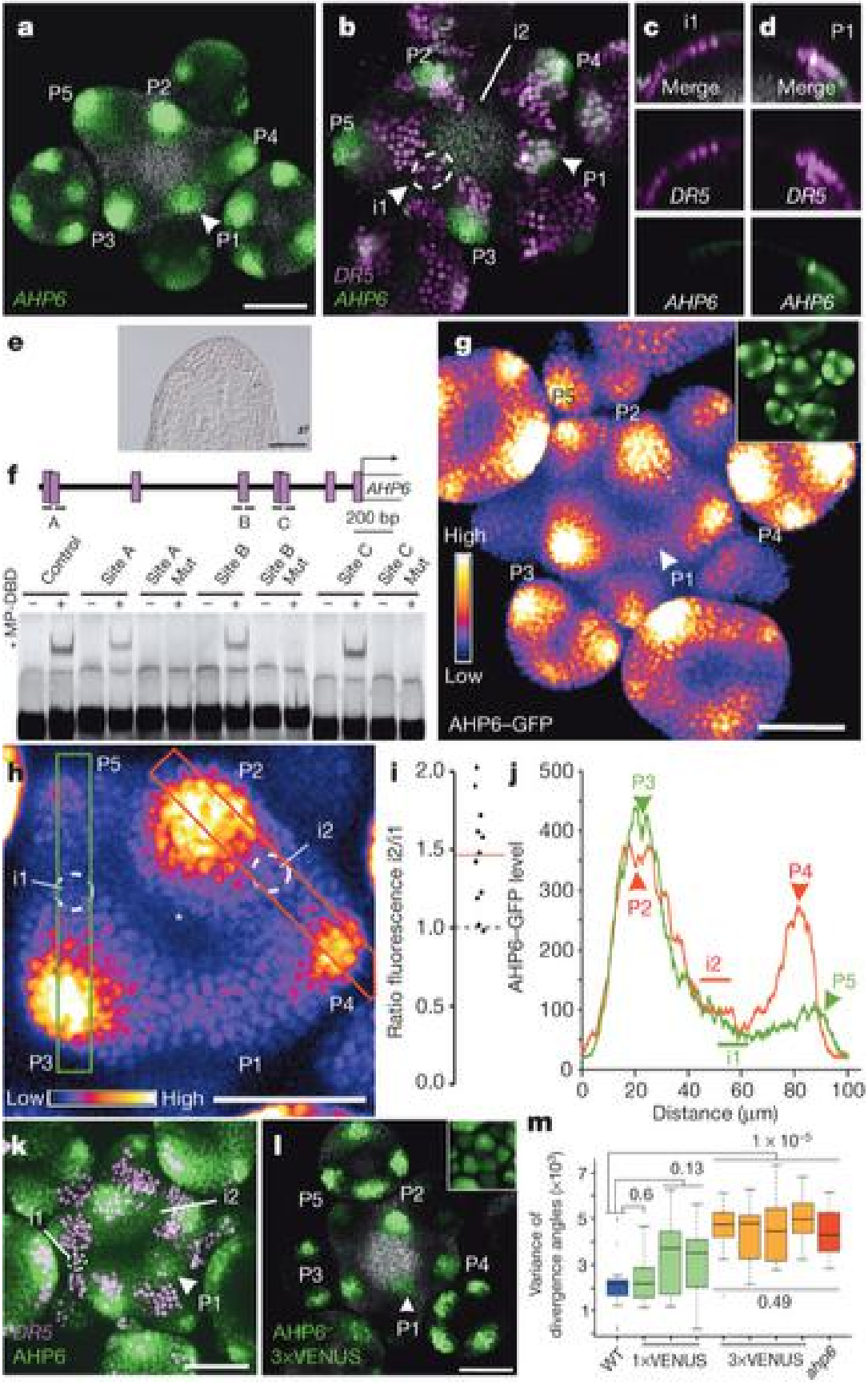

a, *pAHP6::GFP*. **b**, *pAHP6::GFP* (green) and *DR5::VENUS* (magenta; n = 6). **c**, **d**, Longitudinal optical sections at i1 (**c**) and P1 (**d**). **e**, *AHP6* expression in *mp-S319*. **f**, Electrophoretic mobility shift assay (EMSA) using MONOPTEROS DNA-binding domain (MP-DBD). Cartoon shows putative ARF binding sites in *AHP6* promoter (1.6 kb). **g**–**k**, AHP6 protein distribution. **g**, *pAHP6::AHP6–GFP* (n = 12; inset shows original image). **h**, Close-up of (**g**). **i**, i2/i1 AHP6–GFP ratios. **j**, Fluorescence distribution along areas shown in (**h**). **k**, *pAHP6::AHP6–GFP* (green) and *DR5::VENUS* (magenta). **l**, *pAHP6::AHP6–3×VENUS* (inset: *pAHP6::AHP6–VENUS*). **m**, Boxplots of variance per individual of divergence angles between siliques in wild type (n = 19), *ahp6-1 pAHP6::AHP6–VENUS* (n = 23, 19 and 17, respectively), *ahp6-1 pAHP6::AHP6–3×VENUS* (n = 17, 17, 18 and 20, respectively) and *ahp6-1* (n = 18). P values: two-sided Kruskal–Wallis. Autofluorescence visible in grey (**a**–**d**, **l**). Scale bars, 50 μm.

The temporal delay between *DR5* and *AHP6* activation, together with the fact that *AHP6* is required for the earliest steps of organ initiation, indicates that *AHP6* acts non-cell-autonomously on the temporal sequence of organ initiation. We thus monitored the distribution in the SAM of a functional AHP6–GFP protein fusion expressed under the endogenous *AHP6* promoter[14]. We observed sharp gradients of AHP6–GFP centred on primordia and extending beyond their boundaries, indicating that intercellular movement of the protein creates fields of AHP6 around organs (Fig. 3g). AHP6–GFP fluorescence quantification further demonstrated that AHP6 movement creates a non-cell-autonomous differential in AHP6 levels between the predicted i1 and i2 sites (Fig. 3h, i; Supplementary Fig. 11), AHP6 levels being 1.47-fold higher (±0.32 with n = 12 meristems; t-test: one-sided $P = 2 \times 10^{-4}$) at the i2 site. Fluorescence profiles taken through i1 or i2 from the two closest primordia (P3 and P5 or P2 and P4, respectively) further indicate that the proximity of P2 and to a lesser extent P4 allows for the higher AHP6 level at the i2 site (Fig. 3j and Supplementary Fig. 12). These profiles also allowed visualization of changes in AHP6 levels produced by primordia; AHP6 levels increase first and then decrease strongly from P4 onwards (Fig. 3h, j). AHP6 levels at i1 are then lower owing not only to an increased distance between i1 and P3 (P2 being further away), but also to lower AHP6 levels produced by P5. Thus, the differential in AHP6 levels between the i1 and i2 sites, that could also be visualized in plants co-expressing AHP6–GFP and *DR5::VENUS* (Fig. 3k), results from both the geometry of the SAM and dynamic changes in AHP6 levels during flower primordia development. AHP6 movement could be blocked by fusing AHP6 to a triple-VENUS (3×VENUS; Fig. 3l and Supplementary Fig. 13a–c). The AHP6–3×VENUS protein expressed under the endogenous *AHP6* promoter (*pAHP6::AHP6–3×VENUS*) was still functional because it could complement the cell-autonomous loss of protoxylem phenotype in *ahp6* roots (Supplementary Fig. 13d–g)[14]. However, in contrast to *pAHP6::AHP6–VENUS*, *pAHP6::AHP6–3×VENUS* could not complement the *ahp6-1* inflorescence phenotype (Fig. 3m). This suggests that AHP6 movement in the SAM generates a differential in AHP6 levels between i1 and presumptive i2, which is required for sequential organ initiation. Note that a narrow region with a lower level of AHP6 was often observed in the vicinity of the expected i2 position, although the proximity of P2 and P4 limited its size compared to i1 (Fig. 3h, j and Supplementary Fig. 12). Thus, slight errors in i2 positioning can almost abolish the i1/i2 AHP6 differential. This could explain the occurrence of co-initiations even in wild-type meristems.

As *AHP6* functions as a cytokinin signalling inhibitor in the root[14], its spatial distribution in the SAM could create differential cytokinin signalling capacities between i1 and presumptive i2. Indeed, comparison of wild-type, *ahp6* mutants and *35S::AHP6* plants (Fig. 4a) showed

that *AHP6* levels negatively modulate the induction by cytokinin of several primary cytokinin response genes[16, 24, 25] in shoot tissues. Expression of the cytokinin-inducible synthetic reporter *TCS::GFP*[25] was also extended in *ahp6* meristems (Fig. 4b, c), indicating that AHP6 negatively regulates the spatial distribution of cytokinin signalling in the SAM. In addition, we found that *TCS::GFP* and *DR5::VENUS* were activated together during organ initiation in partly overlapping domains in wild-type plants: *TCS::GFP* expression was absent from presumptive i2 but started to be expressed at low levels in i1 and increased in P1 onwards, thus demonstrating a progressive activation of cytokinin signalling (Fig. 4d, f–h, l). In *ahp6* meristems, *TCS::GFP* was on the contrary already expressed in i2 at a level similar to that observed in P1 in wild type and increased further compared with wild type from i1 onwards (Fig. 4e, i–k, l), indicating that AHP6 protein distribution regulates the spatiotemporal pattern of cytokinin signalling during organ initiation. Our results thus show that AHP6 distribution in the SAM creates a differential in cytokinin signalling between i1 (higher cytokinin signalling) and presumptive i2 (lower cytokinin signalling).

Figure 4: AHP6 inhibitory fields generate patterns of cytokinin signalling in the meristem.

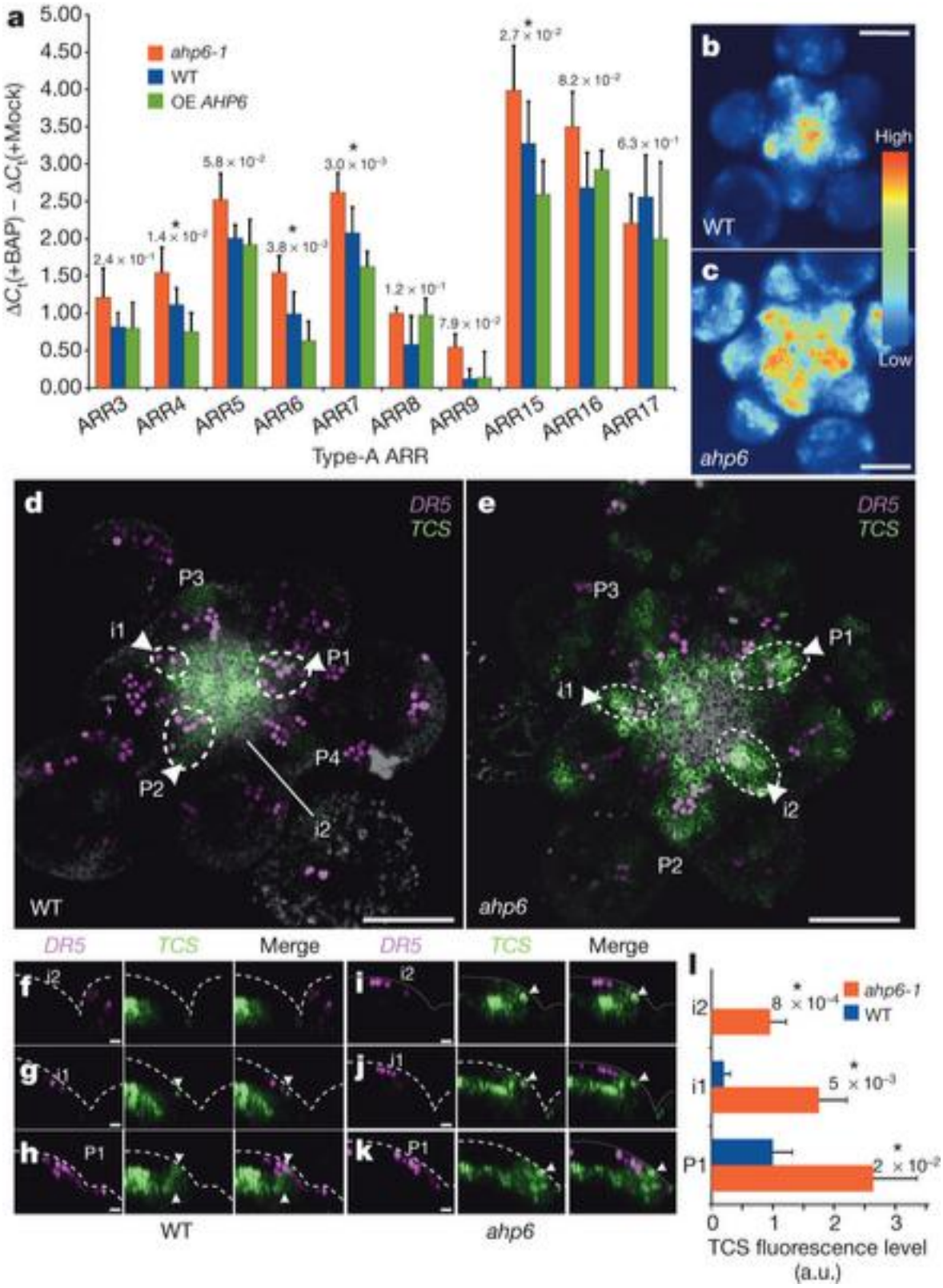

a, qRT–PCR of *ARABIDOPSIS RESPONSE REGULATORS* (*ARRs*) induction by cytokinin (100 nM BAP) in wild-type, *ahp6-1* and *35S::AHP6* (overexpression, OE). *P* value shows two-sided ANOVA (n = 3), $*P$ = 0.05. Error bars show s.d. **b**, **c**, *TCS::GFP* in wild-type (**b**; WT: n = 10) and *ahp6-1* (**c**; n = 9). **d**–**k**, *DR5::VENUS* (magenta) and *TCS::GFP* (green) in

wild type (**d, f–h**) and *ahp6-1* (**e, i–k**). Longitudinal optical section with both merged and separate channels in i2, i1 and P1 are shown (WT: **f–h**; *ahp6-1*: **i–k)**. Arrowheads indicate *TCS::GFP* in primordia; **l**, TCS::GFP quantification. *P* values from one-sided Mann–Whitney *U*-test (WT: $n = 5$; *ahp6-1*: $n = 8$; $*P = 0.05$). Error bars represent s.d. Grey autofluorescence visible (**d**, **e**). Scale bars, 50 μm (**b**–**e**), 10 μm (**f**–**k**).

The negative correlation between AHP6 protein levels and *DR5* levels in i1 and presumptive i2 suggests that the differential in cytokinin signalling generated by AHP6 could act by modulating PIN-regulated auxin transport, as observed in root tissues[22, 26, 27]. However, we could not detect any changes in PIN1 levels or intracellular localization or in PIN1 polarity distribution in the SAM of *ahp6* mutants (Supplementary Fig. 14). This indicates that AHP6 is unlikely to affect auxin transport in the SAM but rather regulates organ initiation after organ positioning by auxin, by acting either in parallel with or downstream of auxin. Consistent with this hypothesis, the downregulation of several cytokinin signalling inhibitors can partially restore organ initiation in the auxin signalling deficient *mp* mutant[28]. A plausible scenario would then be that lower levels of AHP6 in i1 compared to presumptive i2 promote i1 initiation. Inversely, higher concentration of AHP6 in i2 would repress cytokinin signalling and organ initiation, allowing for a time delay between i1 and i2 initiations.

In conclusion, our results indicate that, although the spatial position of new organs at the SAM is robustly determined by the auxin-based inhibitory fields[4, 5 , 9, 10, 11, 12, 13], the dynamics of these fields leads to a noisy plastochron. Accordingly, a recent theoretical study demonstrated that noise induces principally irregularities of the plastochron in a phyllotactic model[29] . Our results further indicate that the noise on the plastochron is then filtered out in part by non-canonical inhibitory fields generated by AHP6 movement downstream of the primary auxin fields. In this scheme, plastochron robustness would be increased by conversion of the spatial information provided by cytokinin signalling inhibitory fields into a roughly periodic temporal sequence of auxin-induced organogenesis (Supplementary Fig. 15).

Plant material and growth conditions

The *ahp6-1*, *ahp6-3*, *mp-S319*, *pLFY::GFP*, *pWUS::GFP*, *pAHP6::GFP*, *pPIN1::PIN1–GFP*, *pAHP6::AHP6–GFP*, *pARR15::GFP*, *DR5::GFP* and *DR5::VENUS* lines have been described[13, 14, 20, 25, 31, 32, 33] and are all in Col-0 except *pLFY::GFP* and *pWUS::GFP* (Ws). All transgenic plants (see below) were generated in the Col-0 ecotype. Plants were grown *in vitro* on Murashige and Skoog (MS) medium or on soil at 20 °C in short-day conditions (8 h light/16 h darkness) for 4 to 5 weeks to synchronize them before being transferred in long-day conditions (16 h light/8 h darkness). Plants showing obvious developmental defects owing to adverse growth conditions were systematically discarded. Plants for live-imaging or for the analysis of phyllotactic sequences were always grown together at the same place within the growth chamber and with randomized position within each tray in order to minimize the effect of environmental fluctuations.

Cloning and constructs

A previously described plasmid[25] was introduced into plants by floral dipping[34] to generate the *TCS::GFP* line. To generate *35S::AHP6*, an *AHP6* full-length complimentary DNA (cDNA) (encompassing a 359-bp 5′ UTR upstream of the ATG and an 83-bp 3′ UTR after the stop codon) obtained by 5′ RACE–PCR was recombined into the Gateway binary vector

dpGreenKanT under the control of the Cauliflower Mosaic Virus (CaMV) 35S promoter. dpGreenKanT was obtained by inserting a Nos terminator after the attR3 recombination site in Kanamycin-resistant version of the Gateway-compatible pGreen 0229 plasmid[35, 36]. The *pAHP6::AHP6–3×VENUS* construct was generated by recombining in phase a 2,429-bp *AHP6* genomic fragment (from 1,594 bp upstream of the ATG to the stop codon), a 2×VENUS without stop codon and VENUS with stop codon into a gateway binary vector pK7m34GW (ref. 37). The plasmids were then transformed into Col-0 and *ahp6-1* plants, respectively, by floral dipping.

Real-time RT–PCR and microarray data analysis

The real-time RT–PCR analysis was designed to comply with standards of qRT–PCR[38, 39] and performed on a StepOne Plus cycler (Applied Biosystems) using the SYBR green reagent kit (Roche). The 7-day-old plants grown *in vitro* were transferred for 24 h on plates containing either mock or 100 nM BAP before extraction of mRNA specifically from the shoot tissues using the Spectrum Plant total RNA kit (Sigma). The primers used are listed in Supplementary Table 1. The *TCTP* gene was used as a standard (Supplementary Table 2) and validated using BestKeeper[40]. PCR efficiency was calculated for each primer pairs using classical calibration dilution curve and used for the estimation of the Ct. Three biological replicates were tested and reactions were carried out using three technical replicates. The effect of the treatment was calculated as the difference between the Ct in the BAP-treated samples and the mock-treated samples (Ct). Statistical significance of the results was tested using an analysis of variance (ANOVA) performed with R (http://www.r-project.org).

For microarray data analysis, expression estimates were calculated from the raw cell files[17] obtained from ArrayExpress using GC robust multi-array average (gcRMA)[41]. Statistical testing for differential expression between the different data sets was performed with LIMMA[42]. Correction for multiple testing was done by computing *Q*-values[43]. These analyses were done under R using Bioconductor packages (http://www.bioconductor.org). By fixing the false discovery rate (FDR) to 1, we identified the following number of genes differentially expressed: FILp-CLV3p: 1379; FILp-WUSp: 1165; CLV3p-WUSp: 1357. Genes affected by protoplasting[17] (592 genes identified) were not considered in the analysis.

Electrophoresis mobility shift assays

The B3 DNA-binding domain of ARF5 (residues 120–274) was cloned into the vector pETM-11 (ref. 44). The protein was produced in *Escherichia coli* strain Rosetta 2 (Novagen) and purified on nickel sepharose high performance media (GE Healthcare) in a buffer containing 20 mM Tris -HCl pH 8.0 and 0.5M NaCl. For EMSA, single-stranded oligonucleotides were annealed to complementary oligonucleotides in annealing buffer (10 mM Tris-HCl pH 7.5, 150 mM NaCl and 1 mM EDTA). The dsDNA (4 pmol) with a protruding G was fluorescently labelled with Cy5-dCTP (8 pmol) (GE Healthcare) using 1 unit of Klenow fragment polymerase (Ozyme) in 1× Klenow buffer for 1 h at 37 °C. Binding reactions were performed with 1.5 µM of purified B3 domain and 25 nM of labelled dsDNA in 20 µl of binding buffer (20 mM HEPES -NaOH pH 7.9, 50 mM KCl, Tris-HCl 100 mM pH 8.0, 1% glycerol, 56 µg fish sperm DNA (Roche)). Binding reactions were loaded onto native 6% polyacrylamide gels and electrophoresis was conducted at 90 V for 75 min at 4 °C in 0.5× TBE (45 mM Tris, 45 mM boric acid and 1 mM EDTA pH 8.0). Gels were further scanned on a Typhoon 9400

scanner (excitation light 649 nm, emission filter 670 nm band-pass filter (670 BP 30); Molecular Dynamics).

The following oligonucleotides were used: TCA (control)

5′-ATACACGCAA**TGTCT**CCCTTTT**TGTCTC**TTCCAC-3′; site A
5′-GCAAAGAAGCAT**GACA**TACGAAT**GAGACA**ATTTCAGTTTT-3′; site A mutated
5′-GCAAAGAAGCAT**GCCA**TACGAAT**GAGCCA**ATTTCAGTTTT-3′; site B
5′-GTTATATGATTATAACTT**GACA**GACCAAATAATCATCTTA-3′; site B mutated
5′-GTTATATGATTATAACTT**GCCC**GCCCAAATAATCATCTTA-3′; site C
5′-AGCTGGTCT**GACA**GGGTACGCCGGT**TGTC**GGGAGGAAGAA-3′; site C mutated
5′-AGCTGGTCT**GCCA**GGGTACGCCGGT**TGGC**GGGAGGAAGAA-3′. The putative ARF binding sites are highlighted in bold and the mutations are underlined.

Cytology and cell biology

To analyse xylem defects in *ahp6-1* mutants expressing AHP6–GFP, AHP6–VENUS and AHP6-3×VENUS, roots of 5-day-old seedlings were cleared with chloral hydrate. RNA *in situ* hybridization on sections was performed as described[2] using full-length probes amplified by PCR. Whole-mount RNA *in situ* hybridization was performed as described[45] except that, before the treatment with proteinase K, permeability of the tissues was increased by digesting cell walls for 4 min at room temperature with an enzyme mix containing 0.5% Macerozyme R10 (Yakult Honsha), 0.5% cellulase RS (Yakult Honsha), 0.25%, pectolyase (Sigma), 0.75% pectinase (Serva) in water further diluted 6 times in PBS with 0.1% Tween20.

For PIN1 whole-mount immunolocalization, inflorescences were first fixed in FAA (5% formaldehyde, 50% ethanol and 10% acetic acid) for 1 h at room temperature (as all subsequent steps, unless specified) and dehydrated by a serial change of 70%, 90% and 100% ethanol (10 min each). Samples were then rehydrated by a serial change of 90%, 70%, 50%, 30% ethanol in microtubule-stabilising buffer (MTSB: 5 mM EGTA, 5 mM MgSO4, pH 7) plus 0.1% Triton and equilibrated with two washes of 10 min in MTSB. The enzyme mix used for whole-mount *in situ* RNA hybridization (see above) was diluted four times in MTSB and cell wall digestion was carried out for 45 min. Samples were then washed 3 times for 10 min in MTSB plus 0.1% Triton. Before antibody application, samples were pre-treated for 1 h in MTSB, 10% DMSO, 3% NP-40 then 1 h in solution A (MTSB, 0.1% Triton, 3% BSA from Sigma). Samples were then incubated overnight at 4 °C with the primary antibody (Ap20 anti-PIN1 antibody (Santa Cruz), dilution 1:100 in solution A), before being washed 4 times for 10 min in MTSB plus 0.1% Triton. Samples were then incubated with the secondary antibody (Alexa 488 antibody from Invitrogen, dilution 1:500 in solution A) for 3 h at 37 °C. The excess of antibody was then removed by 5 washes of 10 min in MTSB plus 0.1% Triton followed by 5 washes in water (10 min each). Samples were then observed using confocal microscopy.

Microscopy and live imaging

SEM was performed as previously described[2]. Cleared roots and RNA *in situ* hybridizations were observed with a transmission microscope under brightfield or differential interference contrast (DIC) illumination (Axio Imager 2, Zeiss). Confocal microscope observations were done either on a LSM-510 laser-scanning confocal microscope (Zeiss), a confocal spinning

disc DMI400 microscope (Leica), a SP5 spectral detection confocal microscope (Leica) or on a LSM-710 spectral laser-scanning confocal microscope (Zeiss). Images were processed using ImageJ (http://rsbweb.nih.gov/ij/). Serial sections were used to count the number of cells expressing *pLFY::GFP* in the younger primordia. Culture and imaging of living SAMs expressing DR5::VENUS was performed as described previously[30] except for adding 555 nM *N*6-Benzyladenine (BAP; Duchefa) in the culture medium. The meristems were allowed to recover for 12 h before starting imaging every 12 h for 72 h. New primordia were scored as co-initiated when they exhibited similar number of VENUS-positive nuclei at a new time point.

Measurements and image analysis

All measurements and image analyses were done using ImageJ (http://rsbweb.nih.gov/ij/). Meristem width was measured on maximum-intensity projections of confocal serial images of living meristems after staining with FM4-64 (ref. 46). For each meristem, the youngest primordium P(n) separated from the meristem by a clear crease was selected. Then, the width was defined as the distance from this boundary to the opposite side of the meristem, located between P(n−1) and P(n−4) (See Supplementary Fig. 6a, b).

For measuring the size of the expression domain of GFP markers (*pWUS::GFP*, *DR5::VENUS*) in the meristem, images for a given marker were thresholded using the same fluorescence intensity range and transformed into binary images. The measure of the area of the central *DR5::GFP* negative region (see Supplementary Fig. 6i, j) was estimated by fitting the largest possible disc between existing primordia expressing DR5::GFP.

The minimal distance of organ initiation to the meristem centre and divergence angle at organ apparition was established using the coordinates of the meristem centre and coordinates of the centre of the initium as soon as the first DR5::VENUS-positive nuclei appeared during the kinetics. Organ displacement was deduced from the evolution of the organ -to-meristem centre distance during the time-lapse imaging. In this analysis, the centre of the meristem was defined as the minimal variation centre of the phyllotactic pattern as described[47]. To obtain the coordinates of the centre in a given image, we either used the FindCenter program (http://www.math.smith.edu/phyllo//Research/findcenter/findcenter.html) or we determined it manually by finding the optimal position giving divergence angles between all organs as close as possible to 137.5°. Both methods gave similar results, but we found that the manual determination was generally more robust. All distances were calculated on projections of serial confocal sections without taking into account the *z* coordinates.

The geometric determination of i1 and i2 positions on meristems was done first by determining the centre of the meristem as described above on a projection of serial confocal sections. Then the centres of all primordia from P4 till the oldest available (typically P8 to P14) were determined. The distance to the centre was then computed for all primordia in order to calculate the plastochron ratios (PR, which is the ratio of the distance to the centre of two consecutive primordia—older divided by younger). A mean PR was calculated for each plant. Then, positions of P3 to i2 were successively calculated at a 137.5° divergence angle from the previous organ (following the handedness of the spiral for the plant analysed) and using the mean PR of the plant to set the distance to the meristem centre. All calculations were performed using GeoGebra (http://www.geogebra.org/cms/fr/). Note that the fit of calculated positions of P3–P1 primordia with their actual positions provided an internal quality control for this geometrical modelling. In addition, the high predictive capacity of this

method for positioning i1 was further demonstrated using 16 *DR5::VENUS* meristems (Supplementary Fig. 11).

For quantification of fluorescence intensities over a region (TCS::GFP or AHP6–GFP), we used summation-intensity projections in the region of interest and calculated the raw integrated density of the fluorescence. For TCS::GFP, we re-sliced the confocal stacks to obtain longitudinal slices of the region corresponding i2, i1 and P1. Fluorescence levels were then measured only from cells in L1 and L2. AHP6–GFP fluorescence levels at the predicted i1 and i2 sites (see above) were also calculated only from L1 and L2 cells over the area of a circle of 100 μm^2 centred on the predicted position of i1 and i2 (this corresponds approximately to the size of i1 when detected with *DR5::VENUS*). Profiles of AHP6 distribution were obtained using the 'Plot Profile' function of ImageJ along the regions indicated on Fig. 3h and Supplementary Fig. 12.

PIN1 transport network analysis

To map PIN1 in the meristems using immunolocalization images, cells were segmented using the Merryproj and Merrysim softwares[48] on the projection of a confocal stack. Influence zones were analysed as described[12]. STSE software was used to process segmentations and PIN1 orientations in order to obtain influence zones, and STSE and PlantGL were used to generate the colour maps[49, 50].

To calculate the PIN1 polarity coherence index for a given cell, we computed all unit vectors pointing from the centre of this cell to the neighbouring cells with a side facing PIN1 proteins. We averaged all these vectors, and normalized the average, so as to obtain a unit vector defining the cell PIN1 polarity, which is representative of the direction in which auxin is transported in the cell of interest. To analyse the coherence of auxin transport, we defined for each cell the average of the polarity vectors of all neighbouring cells (including the cell of interest). The coherence index is the norm of this final average polarity vector. The coherence index has the value 1 when all cells have the same polarity, and a low value if polarities are very different. In order to generate a control, we replaced the measured PIN1 distribution by a distribution in which PIN1 proteins in a given cell are reallocated randomly to the other sides of each cell (and keeping the same number of sides carrying PIN1 so that connectivity remains the same). We recomputed the coherence index for this 'random' PIN1 distribution. Scenarios and index calculations were implemented using Python.

Measures of phyllotactic sequences

Measures of the sequences of silique divergence angles was performed as described[51]. For each phyllotactic measurement, several plants of the different genotype tested were grown in parallel (always including Col-0 and *ahp6-1* control individuals). For each individual of each genotype, the variance of the divergence angles was computed and individual variances of divergence angles were compared between genotype using a non-parametric Kruskal–Wallis test under R, as their distributions were not normally distributed.

Analyses of *ahp6-1 pAHP6::AHP6–VENUS* and *ahp6-1 pAHP6::AHP6–3×VENUS* were performed on T2 transformants which were hemizygote or homozygote for the transgene.

Models used for characterization of permutation patterns

To investigate the presence of particular motifs in phyllotactic sequences, we pooled four independent experiments of measurements with reproducible results, providing a data set of 82 wild-type and 89 *ahp6-1* plants. An exploratory analysis highlighted two characteristics of the divergence angle sequences: (1) the existence of short segments of non-canonical divergence angles along measured sequences (Fig. 1h, i, Supplementary Fig. 4c–f); and (2) almost all the possible angle values between 0 and 360° were observed with highest frequencies around the canonical angle α (Supplementary Fig. 4a). At least four classes of divergence angles were apparent but they were not unambiguously separated. To test if the segments of non-canonical angles could be explained by permutations and given the noisy character of the measurements, we designed a stepwise modelling approach[52, 53] with two objectives: (1) to identify permutation patterns; and (2) optimally label the measured divergence angle sequences.

In a first step, a stationary hidden first-order Markov chain was estimated on the basis of the pooled measured divergence angle sequences (171 sequences representing a cumulative length of 5,220 angles). In this hidden first-order Markov chain, the states of the non-observable Markov chain represents 'theoretical' divergence angles whereas von Mises observation distributions attached to each state of the non-observable Markov chain represents measurement uncertainty. The von Mises distribution[54] is a univariate Gaussian-like periodic distribution for a variable $x \in [0, 360^\circ)$. The von Mises observation distributions estimated for the five states of the non-observable Markov chain were centred on the multiples of the canonical divergence angle α, 2α, −α, 3α, −2α (see Supplementary Table 2). The permutation of 2 consecutive organs generates the divergence angles 2α, −α and 3α. The identification of −2α using this five-state model suggested the occurrence of permutations involving 3 organs in the measured sequences. If in addition to 2-permutations, 3-permutations are considered, the divergence angles −2 α, 4α and 5α are expected to be observed[52] . As the standard deviations of these von Mises observation distributions were quite similar, particularly for the most represented states corresponding to α, 2α and − α, we chose to estimate a five-state hidden first-order Markov chain in which the von Mises observation distributions share the same concentration parameter (inverse variance). The optimally labelled divergence angle sequence (that is, discrete sequence with five possible values chosen among α, 2α, − α, 3α, −2α) was then computed for each observed sequence using the estimated hidden first-order Markov chain.

In a second step, the memories of a variable-order Markov chain were optimally selected[55] on the basis of these labelled divergence angle sequences. This can be interpreted as a way to identify local dependencies between successive divergence angles. For the selection of these memories, we chose to discard the individuals that were very poorly explained by the estimated hidden first-order Markov chain (10 individuals out of 171 whose posterior probability of the optimally labelled divergence angle sequence <0.13). The variable-order Markov chain was a mixed first-/second-order Markov chain where the first-order memory 2α was replaced by the four second-order memories α2α, 2α2α, −α2α, −2α2α (the memory 3α2α was not observed) with respect to a simple first -order Markov chain. This means that to predict accurately the most frequent permutation patterns, it is only necessary to take into account the divergence angle that precedes 2α. This is illustrated by the building of the 2-permutation pattern [2α −α 2α] as a succession of memories with high transition probabilities: $\alpha 2\alpha \xrightarrow{0.91} -\alpha \xrightarrow{0.72} -\alpha 2\alpha$(Supplementary Table 3) instead of $2\alpha \xrightarrow{0.48} -\alpha \xrightarrow{0.71}$with a simple

first-order Markov chain. Finally, a hidden variable-order Markov chain was estimated where the underlying variable-order Markov chain has the memories previously selected.

One advantage of hidden Markov models is the capability to compute an absolute measure of the relevance of the optimally labelled divergence angle sequence as a posterior probability (that is, weight of this optimally labelled divergence angle sequence among all the possible labelled divergence angle sequences that can explain a given observed sequence). One shortcoming of hidden Markov models is that some multiples of the canonical divergence angle that occur rarely (for example, 4α, 5α) as well as alternative phyllotaxis (for example, Lucas with a canonical divergence angle of 99.5°) cannot be modelled. To be able to further investigate these sequences, we used a combinatorial mixture model as described[52]. The final results are then a consensus deduced from the divergence angle sequence optimally labelled by the hidden variable-order Markov chain and the combinatorial mixture model (Fig. 1k).